NOVEL METHOD FOR HIGH-SPEED-LINEAR FUSION PLASMA DIAGNOSTIC BY SIMULTANEOUS DIRECT DETERMINATION OF THE ELECTRON DENSITY AND TEMPERATURE IN THE FUSION REACTOR. THEORY AND SIMULATION

Dimitar Stoyanov[1*], Tanja N. Dreischuh[1] and Angel Popov[2]

[1]*Institute of Electronics, Bulgarian Academy of Sciences,*
72, Tzarigradsko Shosse Blvd, 1784 Sofia, Bulgaria,
e-mails: dvstoyanov@ yahoo.co.uk;

[2]*Institute of Metal Science, Equipment and Technologies*
with Hydro- and Aerodynamics Centre "Acad. Angel Balevski",
Bulgarian Academy of Sciences,
67, Shipchenski Prohod Blvd, 1574 Sofia, Bulgaria,
e-mail: angelsashev@gmail.com

Abstract. This article presents a novel method for high-speed fusion plasma diagnostic based on two specific narrow spectral bands of the total Thomson Scattering (TS) spectra. Two integral conditions are formulated, providing the optical radiation within these spectral bands to be directly proportional to the corresponding basic plasma parameters – the electron density and temperature. A model of a Continuous Wave (CW) Light Detection and Ranging (LIDAR) diagnostic system meeting the expected performance is presented. The direct real-time joint measurements of the electron density and temperature are possible here by fast photodetection, digital sampling and processing of the electrical output signals without using inversion algorithms. The good linearity of the novel method is demonstrated by computer modelling and simulations. The method performance is tested by simulations for the cases of pedestal plasma in the presence of the so-called Edge Localized Modes (ELMs) in the H-mode operation of fusion reactors. Approaches to calibrating instruments are also analysed. The effects of photon numbers fluctuations are considered and error estimates are given as well. Some advantages of the CW TS LIDAR scheme by this method are also discussed. In principle, no limitations exist for the method developed to be applied to fast density and temperature joint measurements inside the plasma core. The overall simplicity of the optical set-up offers a variety of different diagnostic approaches.

[*]Corresponding author.

DOI: 10.7546/EngSci.LIX.22.02.01

Keywords: Thomson scattering, Tokamak, fusion plasma density and pedestal, direct real-time detection of fast processes inside the plasma core.

1. INTRODUCTION

Different diagnostic instruments [1–4] are used in modern fusion reactors for measuring fast plasma variations, such as the electron density and temperature evolutions within the pedestal area, as caused by Edge Localized Modes (ELMs) [5–7].

The fusion plasma electron density profiles are typically probed by MicroWave (MW) radar reflections on free electrons. For example, the Density Profile MW Reflectometers [4–5, 8] measure density profiles inside the plasma with radial resolutions below 1 cm and temporal resolutions within the range of 1 µs–1 ms at an accuracy of $\sim$5%. The Lithium beam instruments for electron density measurements offer a radial resolution of 1.5–2 cm at 20 ms time resolution and can be used for pedestal gradient measurements, as well as in the Scrape-off Layer (SOL) [9–10]. The multichannel heterodyne MW Electron Cyclotron Emission (ECE) Radiometers ensure efficient diagnostics by electron temperature profiling with radial resolutions within 1.5–2 cm on the edge and $\sim$2–4 cm within the core plasma at an accuracy of $\sim$10% and temporal resolutions, typically varying within the range from 0.2–1 ms up to 1 µs for studies of fast processes [1–3].

The Thomson scattering diagnostics is among the most powerful technologies and is based on the measurement of laser-light scattering intensities and relativistic Doppler shifts from free plasma electrons, thus providing simultaneous range profiling of the electron density n_e and temperature T_e [11–12]. The typical measuring accuracies of the Thomson Scattering (TS) Core Light Detection and Ranging (LIDAR) (backscattering geometry) of the Joint European Torus (JET) are $\sim$5% in determining n_e and $\sim$10% in determining T_e at a radial resolution of $\sim$11 cm and a 50 ms time resolution. Similar accuracies are expected to be realized by the ITER TS LIDAR at a radial resolution of $\sim$7 cm and a $\sim$10 ms time resolution [10–12]. Another modification of the TS diagnostics is the High-Resolution Thomson Scattering (HRTS) system, which uses variable scattering geometry with a spatial resolution from $\sim$2.5 cm up to $\sim$1 cm at 20 Hz laser repetition frequency [13]. TS LIDAR systems are used for relative alignment of other diagnostics as well. As a rule, they do not provide reliable information on fast events (say, for ELMs time evolutions) due to the low repetition rates of the laser sources.

Some disadvantages of the above techniques can be here marked: (i) the two plasma parameters are measured by different instruments (excluding the TS diagnostics), leading usually to differences in the sampling rates (time resolutions) of the density and temperature variations; (ii) time-consuming retrieving algorithms are applied to extract the electron density and temperature time dependences; (iii) moreover the non-real-time operation precludes the development of fast feedback controlling techniques, synchronized directly to the electron density and temperature time variations.

In this article, a novel TS method is proposed that can provide high-speed simultaneous measurements of the electron density and temperature. It is based on the specific selection of TS spectral intensities within two defined narrow spectral bands of the total TS spectra. A relatively simple TS optical set-up is analyzed meeting the expected performance by fast photo-detection, direct digitizing and processing of output electrical signals without retrieving algorithms. Further, the residual nonlinear distortions are estimated within the operational electron temperature interval from 0.1 keV to 1 keV, covering the expected ELM time evolution variations in fusion reactors. Some estimates for comparison of Pulsed and CW LIDAR capabilities are discussed as well. Approaches to applying the method to diagnostic instrument calibration are also considered, as well as the effects of Poisson fluctuations in the number of TS photons received.

2. DESCRIPTION OF THE METHOD FOR HIGH-SPEED FUSION PLASMA DIAGNOSTICS

The method proposed is based on the assumption that the TS optical intensities, selected within two well-defined specific narrow spectral bands of the total Thomson Scattering Spectra (TSS), are proportional to the plasma electron density $n_e(t)$ and electron temperature $T_e(t)$, where t is the time. By fast photo-detection of selected spectral intensities, one could generate the corresponding output electrical signals proportional to the two plasma parameters. The direct simultaneous high-speed measurement of $n_e(t)$ and $T_e(t)$ can be then implemented by fast digitizing and processing of the electrical output signals, avoiding the use of inverse algorithms. Determining the TS spectral bands of interest, i.e., those capable of providing electrical signals proportional to the plasma parameters, is of a key importance for the method application. The performance analysis can be fulfilled by computer modelling based on the generally accepted analytical expression for the TS fusion spectra [14–15].

2.1. Block-diagram of the TS diagnostic system

The block-diagram of a possible TS diagnostic system satisfying the requirements for direct fast simultaneous determination of both plasma parameters considered is presented in Fig. 1. The plasma electrons are irradiated by a CW laser radiation. This scheme offers a lot of advantages with respect to pulsed TS LIDARs at probing the pedestal area, containing ELMs. The radiation of a CW laser 1 is focused on a defined distance z from the torus wall 2 within the pedestal area. The distance z defines also the position of the system resolution volume dz in the horizontal direction. The parameter dz depends on the laser beam angular divergence as well as on parameters of the optics. The resolution volume is assumed to be of order of the pedestal width $z_{ped} \sim 4 - 5$ cm or $\delta z \sim z_{ped}$. Using the focusing scheme of the CW LIDAR in Fig. 1 one could avoid time of flight measurements by short laser pulses. It is evident the CW LIDAR scheme can be effective at a presence of a single resolution volume dz of independently known position z (the ELM pedestal). Moreover, the CW laser 1 in Fig. 1 is assumed to be equipped with an optical attenuator for a precise remote controlling of the total output laser radiation.

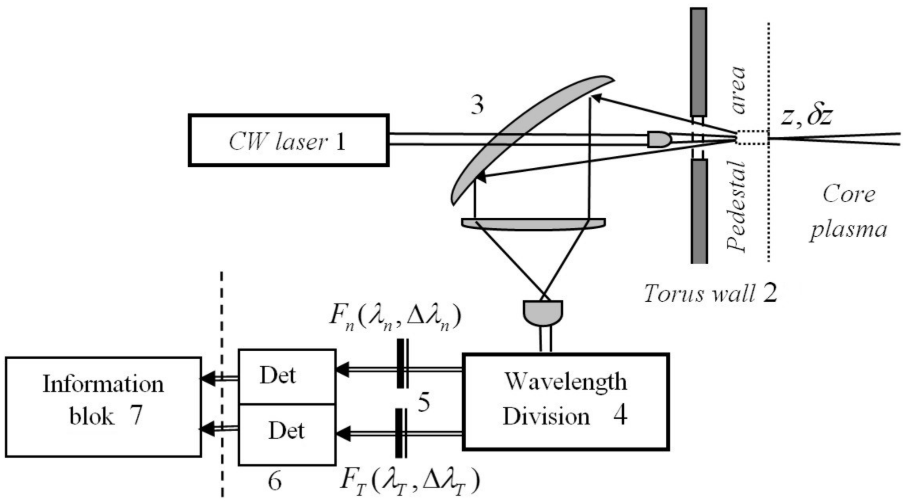

Fig. 1. Block-diagram of a TS diagnostic system for direct measurement of plasma electron density and temperature

The backscattered Doppler-shifted radiation from the relativistic free plasma electrons inside the plasma resolution volume dz is collected by the receiving optics 3 and then directed through a wavelength division unit 4 to a set of two filters of defined shapes 5: $F_n(\lambda_s) = F_n(\lambda_i, \lambda_s, \lambda^n_{\max}, \Delta\lambda_n)$ for the electron density measurement (n_e-channel) and $F_T(\lambda_s) = F_T(\lambda_i, \lambda_s, \lambda^T_{\max}, \Delta\lambda_T)$ for the electron temperature measurement (T_e-channel). Here indices n and T denote the parameters linked to both the n_e and T_e channels, respectively, λ_i is the incident laser wavelength; λ_s is the TS radiation wavelength; $\lambda^n_{\max}$, $\lambda^T_{\max}$ are the filters maximum transmission wavelengths; $\Delta\lambda_n$, $\Delta\lambda_T$ are their corresponding bandwidths (FWHM). The selected radiations in two spectral band widths $\Delta\lambda_n$, $\Delta\lambda_T$ are photo-detected in analogue mode and amplified by corresponding units 6. Further, the electrical output signals from units 6 are sampled by the Analogue-to-digital Converters (ADCs) with a time step τ_s and further processed in real time (block 7). The time resolution of the system is equal to the sampling step τ_s. Moreover, the entire system in Fig. 1 is assumed to be digitally controlled by the information block 7 as well.

For simplicity, we will use further the joint notation $F_{n,T}(\lambda_s)$ of the two filter shapes $F_n(\lambda_s)$ and $F_T(\lambda_s)$, indexed by n and T, respectively. Let us denote the numbers of backscattered photons by $L^{ph}_n(t)$ and $L^{ph}_T(t)$ detected for resolution time τ_s in the n_e and T_e channels of the optical system, respectively. As above, we will use for simplicity the joint notation $L^{ph}_{n,T}(t)$. The quantities $L^{ph}_{n,T}(t)$ are expressed by the LIDAR equation for the case of a TS LIDAR system emitting CW laser radiation [15–16], or:

$$L^{ph}_{n,T}(t) = K_{n,T} N_0(\lambda_i) \tau_s n_e(t, z, \delta z) \\ \times \int_{\lambda_s} F_{n,T}(\lambda_s)\, Tr_c(\lambda_s)\, EQE(\lambda_s)\, T_{sp}\left[T_e(t, z), \lambda_i, \lambda_s\right] d\lambda_s, \quad (1)$$

where $N_0(\lambda_i)$ is the photon rate of the incident laser radiation; $n_e(t, z, \delta z)$ is the total electron density within the illuminated plasma volume δz at a distance z; $T_{sp}\left[T_e(t, z), \lambda_i, \lambda_s\right]$ is the normalized TS spectrum for a given electron temperature $T_e(t, z)$ [14–15]; $Tr_c(\lambda_s)$ are the transmissions of the collection paths; $EQE(\lambda_s)$ are the effective quantum efficiencies; $K_{n,T}$ are general constants for the n_e and T_e channels, which depend on the system non-wavelength dependent factors, the receiving optics parameters, the plasma-volume backscattering coefficient, etc.

Now, let us assume (in a first order of approximation) that the bandwidths of filters $F_{n,T}(\lambda_s)$ are narrow with respect to the typical broadband transmissions of the collection paths $Tr_c(\lambda_s)$, as well as to the effective quantum efficiencies. Assuming $Tr_c(\lambda_s) \approx \text{const}$, and $EQE(\lambda_s) \approx \text{const}$ within the corresponding filter bandwidths $\Delta\lambda_{n,T}$, the output signals detected $S^{out}_{n,T}(t)$

are given by:

$$S_{n,T}^{out}(t) \sim C_{n,T} L_{n,T}^{ph}(t) \sim n_e\,(t) \int\limits_{\lambda_s} F_{n,T}\,(\lambda_s) T_{sp}\,[T_e(t), \lambda_i, \lambda_s]\, d\lambda_s, \tag{2}$$

where $C_{n,T}$ are constants and $T_e\,(t) = T_e(t,z)$, $n_e\,(t) = n_e(t,z)$.

2.2. Integrals providing the linear performance

Following the declared goals of generating electrical signals $S_{n,T}^{out}(t)$ corresponding to the plasma parameters considered, let us assume the integral in equation (2) to be proportional to the variations of the electron plasma temperature $T_e\,(t)$ within a defined operational temperature range from $T_e^{\min}$ to $T_e^{\max}$, when using the filter $F_T\,(\lambda_s)$, or:

$$\int\limits_{\Delta\lambda_T} F_T(\lambda_s) T_{sp}\,[T_e(t), \lambda_i, \lambda_s]\, d\lambda_s \sim T_e\,(t)\,, \tag{3}$$

where $T_e\,(t) = \bar{T}_e + \Delta T_e\,(t)$, $\bar{T}_e$ is the mean temperature and $\Delta T_e\,(t)$ are variations centered within the defined temperature range. Assuming the condition (3) to be fulfilled, one will obtain from equation (2) the intermediate signal $S_p^{out}(t)$ as expressed by:

$$S_p^{out}(t) = c_0 n_e\,(t)\, T_e\,(t)\,, \tag{4}$$

where $c_0 = \text{const}$. The next step is to describe the generation of an electrical output signal $S_n^{out}(t)$ proportional to the electron density within the same electron temperature interval ($T_e^{\min} \div T_e^{\max}$). To this purpose, we should define the filter $F_n\,(\lambda_s)$ in such a way that:

$$\int\limits_{\Delta\lambda_n} F_n\,(\lambda_s) T_{sp}\,[T_e(t), \lambda_i, \lambda_s]\, d\lambda_s = \text{const}. \tag{5}$$

As a result, we will obtain from equation (2) an output signal that is linearly dependent on the electron density:

$$S_n^{out}(t) = c_n' n_e\,(t)\,, \tag{6}$$

where $c_n' = \text{const}$. Then, the output signal $S_T^{out}(t)$, proportional to $T_e\,(t)$, is determined by dividing signals (4) and (6) and thus:

$$S_T^{out}(t) = \frac{S_p^{out}\,(t)}{S_n^{out}\,(t)} = \frac{c_0 n_e\,(t)\, T_e\,(t)}{c_n' n_e\,(t)} = c_T' T_e\,(t)\,, \tag{7}$$

where $c'_T = \text{const}$. In equation (7) we assumed the inequality $n_e(t) > 0$ to be fulfilled in the H-mode within the temperature range $T_e^{\min} \leq T_e(t) \leq T_e^{\max}$. Moreover, the intermediate signal $S_p^{out}(t)$ in equation (4) could be useful in some experimental data analyses, as it is also directly proportional to the product of the electron density and temperature (or the electron pressure in non-magnetized plasma). From a physical point of view, the linear dependences (6) and (7) are produced by the combined effects of the TS spectra complex shapes and the filter spectral characteristics at electron temperature variations within the operational interval.

3. COMPUTER MODELLING AND SIMULATION RESULTS

In this section, we present a set of basic simulation results from computer modelling of the novel instrument performance. Special attention will be paid to the following topics: (i) determination of specific spectral shapes of filters $F_T(\lambda)$ and $F_n(\lambda)$ within the defined interval $T_e^{\min} \leq T_e(t) \leq T_e^{\max}$; (ii) estimation of nonlinear distortions of signals $S_n^{out}(t)$ and $S_T^{out}(t)$ as functions of the input density $n_e(t)$ and temperature $T_e(t)$, respectively; (iii) calibration of the detected and sampled output signals; (iv) fluctuation effects in the number of photons received.

The computer model is based on expression (1) for the number $L_{n,T}^{ph}(t)$ of backscattered photons detected in the two channels. The relativistic Thomson scattering spectra $T_{sp}[T_e(t,z), \lambda_i, \lambda_s]$ are calculated from the theoretical model for the case of backscattering geometry [15–16]. The simulation code contains a set of moduli allowing calculation and estimation of instrument blocks presented in this article, such as filter shapes, calibration procedures, etc. As an example of applying the method, we will demonstrate its satisfactory performance within a temperature interval interesting from the point of view of high-speed measurement of ELM time evolution on the edge of a Be-walls torus (as in JET). The input density and temperature temporal variations are modelled so as to be similar to typical ELM time evolutions, as measured by some diagnostic instruments (see below). It is further assumed that the ELM time evolution series are (in the first order of approximation) stationary processes within measuring intervals t_{meas} much longer than the characteristic time duration τ_{ELM} of the ELM pulses ($t_{meas} \gg \tau_{ELM}$). This requirement is fulfilled (see below) for relatively short measuring intervals $t_{meas} \ll \tau_H$, τ_H being the H-mode.

3.1. Determination of the optical filters spectral shapes

In the calculations we used a simple mathematical model for the two filters $F_{n,T}(\lambda_s)$ that contains sets of well-defined variable parameters. In general, the filter shapes contain two flat wings on both the sides of the central wavelengths $\lambda_{\max}^{n,T}$ and two wavelength dependent wings of $(1-0.5\mathrm{cosine}(\lambda_s))$ type, disposed on both the sides of the flat wings. They are denoted as follows: (i) positions of the corresponding central wavelengths $\lambda_{\max}^{n,T}$; (ii) widths of the left- $w_l^{n,T}$ and right-hand $w_r^{n,T}$ sides of the filters plateaus with respect to $\lambda_{\max}^{n,T}$; (iii) widths of the filters left- $v_l^{n,T}$ and right-hand $v_r^{n,T}$ wings (wavelength dependent) outside the plateaus. The mathematical expressions are:

$$F_{n,T}(\lambda_s)=\begin{cases} 1-0.5\cos\left(\pi(\lambda_s-\Lambda_l^{n,T})\Big/v_l^{n,T}\right) \\ \qquad\qquad \text{for } \lambda_l^{n,T}\le\lambda_s\le\lambda_l^{n,T}+v_l^{n,T} \\ \\ 1 \qquad\qquad \text{for } \lambda_{\max}^{n,T}-w_l^{n,T}<\lambda_s<\lambda_{\max}^{n,T}+w_r^{n,T} \\ \\ 1-0.5\cos\left(\pi(\Lambda_r^{n,T}-\lambda_s)/v_r^{n,T}\right) \\ \qquad\qquad \text{for } \lambda_r^{n,T}-v_r^{n,T}\le\lambda_s\le\lambda_r^{n,T} \end{cases}, \tag{8}$$

where $\Lambda_l^{n,T}=\lambda_{\max}^{n,T}-w_l^{n,T}-v_l^{n,T}$ and $\Lambda_r^{n,T}=\lambda_{\max}^{n,T}+w_r^{n,T}+v_r^{n,T}$. The spectral shapes selected of $F_{n,T}(\lambda_s)$ are presented in Fig. 2(a) together with the laser line λ_i, as well as the TS spectra $T_{sp}\left[T_e^{\min},\lambda_i,\lambda_s\right]$ and $T_{sp}\left[T_e^{\max},\lambda_i,\lambda_s\right]$ calculated for the boundary electron temperatures $T_e^{\min}$ and $T_e^{\max}$, respectively.

As seen, the filter characteristic of $F_T(\lambda_s)$, satisfying the requirement for linear dependence of the integral in equation (3), is situated on the left-hand side (blue shift zone) with respect to the TSS maxima along the operational interval. This position of $F_T(\lambda_s)$ provides for the method good sensitivity, because of the steeper TS spectra decrease at lower wavelengths and a higher $T_e(t)$. The filter shape $F_n(\lambda_s)$, satisfying the condition for the integral in equation (5) to be constant within the same interval $(T_e^{\min}\div T_e^{\max})$, is situated on the right-hand side of the laser wavelength λ_i (red shift zone). The position of $F_n(\lambda_s)$ on the λ-axis is also well grounded, as for any electron temperature with the interval $(T_e^{\min}\div T_e^{\max})$, the TS spectra in the red zone will cover narrower spectral intervals with respect to the blue zone. It offers the opportunity to use a relatively narrow bandwidth filter of a steep left wing to collect practically the total scattered radiation within the red zone for any electron temperature within the operational interval. The requirements that both conditions (3) and (5) should hold true are provided by tuning the variable

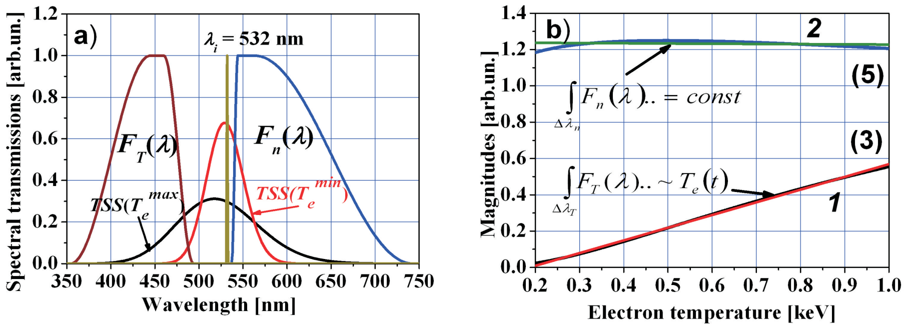

Fig. 2. (a) Selected spectral shapes of filters $F_{n,T}(\lambda)$; (b) Temperature dependences of the integrals in equations (3) and (5) for the corresponding spectral shapes $F_{n,T}(\lambda_s)$

parameters into equations (8). The parameters of the two filters selected are summarized in Table 1 for $\lambda_i = 532$ nm (2^{nd} harmonic of the Nd:YAG-laser).

Table 1. Selected numerical parameters according to equations (8), providing the requirements to both conditions in equations (3) and (5)

$F_T(\lambda_s)$	$\lambda^T_{\max} = 448$ nm	$w^T_l = 3$ nm	$w^T_r = 12$ nm	$v^T_l = 91$ nm	$v^T_r = 34$ nm
$F_n(\lambda_s)$	$\lambda^n_{\max} = 562$ nm	$w^n_l = 18$ nm	$w^n_r = 1$ nm	$v^n_l = 7$ nm	$v^n_r = 180$ nm

The dependences of the two integrals in equations (3) and (5) on the temperature variations within the interval ($T_e^{\min} \div T_e^{\max}$) are of key importance for the method performance. Using the filter characteristics selected, given in Table 1, we calculated the above integrals as functions of $T_e(t)$. The results are plotted in Fig. 2(b), where curves 1 and 2 display the values of the integrals in equations (3) and (5), respectively. The fits of both curves are given as well. It is seen that the linearly fitted curves 1 and 2 overlap well with the values of the integral within the interval from 0.2 keV to 1 keV. The differences between the values of the integral and the fitting results do not exceed $\pm 1\%$, for curve 1, and $\pm 4\%$, for curve 2.

We analysed also the residual effects of the spectral dependence of the effective quantum efficiencies $EQE(\lambda)$ on the integrals in Fig. 2(b) in the case of using the filters $F_{n,T}(\lambda)$ already tuned as given in Table 1. As expected, the effects of $EQE(\lambda)$ are too low because of their much wider bandwidths with respect to the narrow spectral bands of filters $F_{n,T}(\lambda)$; thus, these effects can be neglected.

3.2. Estimation of the output signals linearity dependence on the electron density and temperature

In this section we will estimate the deviations from linearity of the signals $S_{n,T}^{out}(t)$ in equations (6) and (7) as functions of the input plasma parameters, when using the filters $F_{n,T}(\lambda)$ of spectral shapes determined by equation (8) and Table 1. The nonlinear distortions arise mainly from the TS spectra nonlinearity within the operational electron temperature interval, as well as from the nonlinear shapes of $F_{n,T}(\lambda)$ within their spectral bands. The total nonlinear distortion factor $K_D \sim sqrt\left((a_2^2)+(a_3^2)+(a_4^2)\ldots\right)/a_1$ is a generally accepted criterion for the linearity of different instruments (a_1 is the amplitude of the basic harmonic and a_2, a_3, a_4 are the amplitudes of the successive higher harmonics [17]). This approach can be applied, if harmonic functions are used as mathematical models of the input electron density $n_e^{inp}(t)$ and temperature $T_e^{inp}(t)$, as given below:

$$n_e^{inp}(t) = \bar{n}_e\left(1 + b_n \sin\left(\omega_n t + \varphi_n\right)\right), \quad T_e^{inp}(t) = \bar{T}_e\left(1 + b_T \sin\left(\omega_n t\right)\right), \tag{9}$$

where ω_n is the basic harmonic frequency of the density and temperature time variations; φ_n is a phase accounting for possible phase delays between $n_e^{inp}(t)$ and $T_e^{inp}(t)$; b_n and b_T are their amplitudes, respectively. Calculating the distortion factors $K_{n,T}$ in both channels involves determining the Fourier spectra of the output signals $S_{n,T}^{out}(t)$ at given plasma variations in equation (9). The nonlinear distortions thus calculated of the density signal $S_n^{out}(t)$ do not exceed $K_n \pm 3\%$ for of the phase delays variations φ_n within the entire range of $\pm\pi$ ($K_n \leq 1\%$ for $\varphi_n \sim 0$). The nonlinear distortion factors K_T of the temperature signal $S_T^{out}(t)$ are of the same order $K_T \sim K_n$ for any φ_n within the entire interval $(-\pi \div \pi)$ as well. These estimates of $K_{n,T}$ can be accepted as tolerable for ELM evolutions measurements. It may be concluded that the TS spectral intensities, selected by filters $F_{n,T}(\lambda)$ within the spectral bands in equation (8) and Table 1, provide the linear performance expected by the method proposed at a low level of nonlinear distortions.

Let us now present the input plasma density $n_e^{inp}(t)$ and temperature $T_e^{inp}(t)$ by:

$$n_e^{inp}(t) = \Delta n_e^{inp}(t) + \bar{n}_e^{inp} \quad \text{and} \quad T_e^{inp}(t) = \Delta T_e^{inp}(t) + \bar{T}_e^{inp}, \tag{10}$$

where $\bar{n}_e^{inp}$ and $\bar{T}_e^{inp}$ are mean values and $\Delta n_e^{inp}(t)$ and $\Delta T_e^{inp}(t)$ are the centered variations. Because of the method linearity, similar expressions could be signals written now for the output signals detected:

$$S_n^{out}(t) = \Delta S_n^{out}(t) + \bar{S}_n, \tag{11a}$$

$$S_T^{out}(t) = \Delta S_T^{out}(t) + \bar{S}_T, \tag{11b}$$

where $\bar{S}_n$, $\bar{S}_T$ are the mean output values and $\Delta S_n^{out}(t)$, $\Delta S_T^{out}(t)$ are the centered output variations. However, as the output electrical signals pass through the various electronic units as amplifiers, the information for the zero values of $\bar{n}_e^{inp}$ and $\bar{T}_e^{inp}$ may be lost or the mean values $\bar{S}_n$ and $\bar{S}_T$ could be shifted with respect to actual mean values. Therefore, the expressions for the output signals should be rewritten in the more correct form:

$$S_n^{out}(t) = c_n \Delta n_e^{inp}(t) + \bar{c}_n \bar{n}_e^{inp}, \tag{12a}$$

$$S_T^{out}(t) = c_T \Delta T_e^{inp}(t) + \bar{c}_T \bar{T}_e^{inp}, \tag{12b}$$

where $\bar{c}_n$ and $\bar{c}_T$ are coefficients for the mean output values. It is evident that the information on the input densities and temperatures fast variations is contained in the centered variations:

$$\Delta S_n^{out}(t) = c_n \Delta n_e^{inp}(t)\,, \tag{13a}$$

$$\Delta S_T^{out}(t) = c_T \Delta T_e^{inp}(t)\,. \tag{13b}$$

3.3. Output signal calibration

The output signals into equations (12a, b) are intermediate products that require application of proper calibration procedures to determine the unknown coefficients $c_n, \bar{c}_n$ and $c_T, \bar{c}_T$. Different calibration approaches could be proposed to be used in real measurements in fusion reactors. Here we will not include an analysis of the contributions of the absolute errors of the calibrating data used, considering this as remaining out of this article scope. Our goals here are to estimate the relative calibration errors of the method proposed with respect to some independently-measured electron density $n_e^{cal}(t)$ and temperature $T_e^{cal}(t)$ data suitable of being used as calibrating data. Below we will only consider a simple calibration procedure, based only on the method linear performance, in order to demonstrate a possible calibration approach. It is accepted further the sample presentations for all variables in equations (10)–(13) because they are to be subjected to further digital processing by the information system. To this purpose it was assumed that the typical requirements to time series are fulfilled according to the sampling theorem in [18]. As an example, let us consider a relative calibration of sampled output signals $S_{n,T}^{out}(k_s\tau_s)$, $k_s = 1, \ldots, K_s$, within the pedestal area by two of the well-known diagnostic techniques, noted above: (i) MW Reflectometer, measuring the

ELM evolution of the electron density $n^r_{e,cal}(k_r\tau_r)$, $k_r = 1,\ldots,K_r$; (ii) MW ECE Radiometer, measuring the ELM evolution of the electron temperature $T^{ec}_{e,cal}(k_{ec}\tau_{ec})$, $k_{ec} = 1,\ldots,K_{ec}$. Accepting these calibrated series $n^r_{e,cal}(k_r\tau_r)$ and $T^{ec}_{e,cal}(k_{ec}\tau_{ec})$ as the input data for the computer model developed here, one can calculate the parameters of the output signals $S^{out}_{n,cal}(k_s\delta\tau_s)$, $S^{out}_{T,cal}(k_s\delta\tau_s)$ passing through the model. Then, the relative calibration errors with respect to the input data could be estimated by comparing them with the output time series.

The simplest calibration by the above approach could be based on the assumption for stationary electron density and temperature time series. Equality of the sampling steps is not mandatory here. As evident, one can calculate the standard deviations $\sigma^n_{e,cal}$ of $\Delta n^r_{e,cal}(k_r\tau_r)$ and $\sigma^T_{e,cal}$ of $\Delta T^{ec}_{e,cal}(k_{ec}\tau_{ec})$ of the calibrating input data, as well as the corresponding standard deviations δ^n_e of $\Delta S^{out}_n(k_s\tau_s)$ and δ^T_e of $\Delta S^{out}_T(k_s\tau_s)$ of the output signals. The calibration procedure can be reduced to comparing the calculated statistical parameters of the output signals $S^{out}_n(k_s\tau_s)$ and $S^{out}_T(k_s\tau_s)$ before the calibration with the corresponding statistical parameters of the calibrating series. One can write the following calibration expressions for the output time series:

$$S^{out}_{n,cal}(k_s\tau_s) = \Delta S^{out}_n(k_s\tau_s)\frac{\sigma^n_{e,cal}}{\delta^n_e} + \bar{n}^{cal}_e, \tag{14a}$$

$$S^{out}_{T,cal}(k_s\tau_s) = \Delta S^{out}_T(k_s\tau_s)\frac{\sigma^T_{e,cal}}{\delta^T_e} + \bar{T}^{cal}_e, \tag{14b}$$

where $S^{out}_{n,cal}(k_s\tau_s)$ and $S^{out}_{T,cal}(k_s\tau_s)$ are the calibrated estimates of the electron density and temperature time series, respectively.

The applications of equations (14a, b) are demonstrated in Fig. 3, where the calibrated output signals $S^{out}_{n,cal}(k_s\tau_s)$ and $S^{out}_{T,cal}(k_s\tau_s)$ are overlapped with the corresponding calibrating electron density and temperature series. The time series in Fig. 3 are stationary processes, at least in the first order of approximation. The Poison fluctuations in the output signals are not included into equations (14). Their effects are given below. The advantages of the calibration expressions (14) are in the use of only two statistical estimates of the calibrating time series: the mean values and the standard deviations. The time histories of the calibrating input series are not used in the calibration procedures. The temporal resolution of the calibrated output signals remains equal to the sampling step τ_s of the output signals after photo-detection.

The relative calibration errors are found to be ~0.7% for the density and 0.3% for the temperature due mainly to residual nonlinearities of the method

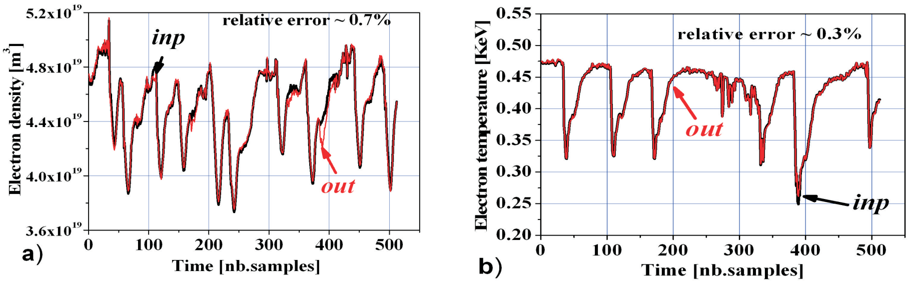

Fig. 3. Application of expressions (14) to the calibration of: (a) electron density; (b) electron temperature time series. The calibrated time series (red) of the density and the temperature are overlapped on the corresponding calibrating series (black)

and could be neglected in the first order of approximation. These advantages offer flexible opportunities for calibration of output signals by the various calibrated diagnostic instruments used in fusion reactors.

3.4. Effects of the Poisson fluctuations on received photons

As well known, the number of photons detected per resolution time in any TS instrument is as a rule low, causing additional errors in the plasma parameters measured. Their estimation requires Monte–Carlo simulations [18]. The typical approach is based on equation (1) for the number of photons $L^{ph}_{n,T}$ detected within the resolution interval τ_S. For a preset $L^{ph}_{n,T}$, one can calculate the output signals fluctuations by using the single parametric Poisson distribution. The effects of Poisson fluctuations on the output signals in the case of a low number of detected photons are illustrated in Fig. 4 for the electron density and temperature time series, where the output series are calibrated (see below).

As seen, the output signals are noisier with relative errors of the order of $\sim$3% at $L^{n,T}_{ph}$ $\sim 10^3$ photons detected per resolution time. The estimated shifts $d\bar{S}_{n,T}$ of the mean values $\bar{S}_{n,T}$ in Fig. 4 resulting from Poisson fluctuations are too low (of the order of $d\bar{S}_{n,T} \sim 10^{-9}\bar{S}_{n,T}$) and, thus, can be neglected.

As seen in Fig. 4 the Poisson fluctuations contribute mainly to the centered variations in the output ELM evolution signals, carrying out the useful information on the fast plasma processes. A mathematical expression of the output signals that account for Poisson noise can have the form (see equation 11):

$$S^{out}_{n,T}(k_s\delta\tau_s) = \Delta S^{out}_{n,T}\,(k_s\tau_s) + \Delta S^{pois}_{n,T}\,(k_s\tau_s) + \bar{S}_{n,T}, \tag{15}$$

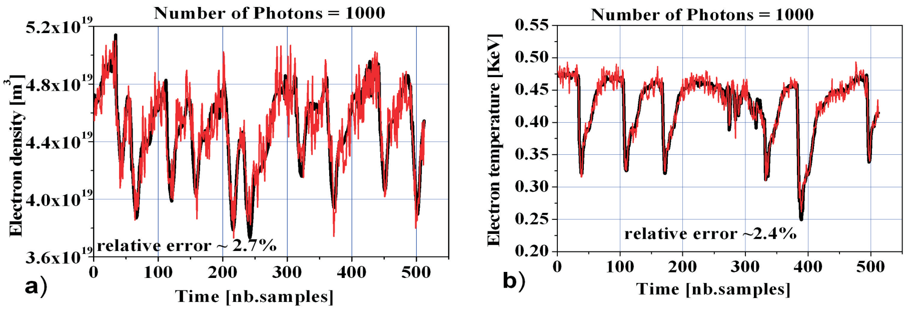

Fig. 4. Calibration using expressions (14) after modification using model (15) for accounting of Poisson fluctuations at low number of photons (1000 mean photons/resolution cell): (a) density; (b) temperature. The Poisson noises are well seen in calibrated output series (red), overlapped on the calibrating series (black)

where $\Delta S_{n,T}^{pois}(k_s\tau_s)$ are the Poisson centered variations with standard deviations denoted below by $\delta_{n,T}^{pois}$ for the electron density and temperature. The calibration expressions accounting for Poisson fluctuations are obtained from equation (14) by replacing $\delta_e^{n,T}$ with $\sqrt{\left(\delta_e^{n,T}\right)^2+\left(\sigma_{n,T}^{Pois}\right)^2}$. The plots of the relative Poisson errors vs the number of photons $L_{n,T}^{ph}$ per resolution cell, varying within a wide range (from 10^2 to 10^4 photons), are displayed in Fig. 5 for both the calibrated electron density and temperature output signals. It can be seen that for $L_{ph}^{n,T}\sim 400$ photons, the relative Poisson error is of the order of $\sim 5\%$, as expected from the standard Poisson distribution. The values of $L_{n,T}^{ph}$ depend on the system optical parameters (laser power, collecting optics, detectors, etc.).

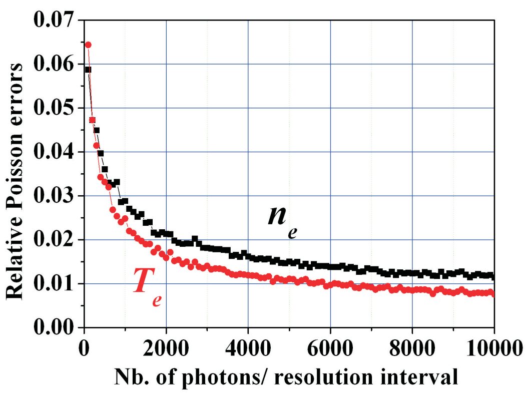

Fig. 5. Plots of Poisson errors vs the number of photons per resolution cell, varying within the wide range from 10^2 to 10^4 photons for both the electron density and temperature channels

An estimate of the necessary CW laser power P_{CW} by this method could be approximately obtained by the assumption that equal numbers of emitted photons of equal wavelengths from the CW and Pulsed TS LIDARs will provide approximately the same numbers of TS backscattered photons from the same plasma volume of same parameters during their accumulation (resolution) times τ_s and τ_p (pulse duration), respectively. Such equality can also be expressed by the equality of energies emitted during both the resolution times. Typically, the emitted energies in pulsed TS LIDARs are of order of $\sim$1 J within the pulse duration. The same energy of 1 J can be emitted by the CW laser of output power P_{CW} $\sim$100 W within an interval $\tau_s = 10^{-2}$s (10 ms). In this case the time resolution τ_s will be of order of the expected limiting resolution, if using the ITER Core TS LIDAR at 100 Hz laser repetition rate. CW lasers of such output CW power (say, Nd:YAG laser, $\lambda_i = 532$ nm) are produced by industry for many years.

3.5. Effects of stray light and background radiation

Let us now discuss the expected noise levels by different noise sources as the background and stray light radiation, if using the CW TS LIDAR scheme. It must be noted the strong spatial selection by the focussing receiving system of the CW LIDAR. Really, the parasitic light beams of both the noise types illuminating the detector sensitive surface have to pass through the small system resolution volume δz (positioned on a defined distance z) under relatively narrow angle (with respect to the optical axis) in order to pass then through the narrow diaphragm before photodetectors. These requirements are valid here for both the noise sources. Moreover, the light beams just after the focus are distributed within large solid angles inside the torus due to the defocusing. This results in additional reduction of stray light intensities, reaching photodetectors. Moreover, both the specific filters $F_{n,T}(\lambda)$ used by the novel method are quite narrower ($\sim$ 75 nm for T_e and $\sim$100nm for n_e at FWHM) with respect to the full spectrum of the plasma background (as the last is received and processed in wider spectral bands of the total TS spectrum by the Pulsed LIDAR). Thus, the combination of larger integration times (CW LIDAR) with narrower receiving bandwidths by the novel method will contribute to the additional reduction of background effects in output ELMs signals.

As shown above (say, equations 12) the information on the densities and temperatures ELMs fast variations is contained in the centered variations. Let us now approximately estimate the *SNRs* by both the methods, denoting by $S^{elm}_{n,T}(\tau_s)$ the centered ELMs output signals in n_e and T_e channels during the integration time τ_s, and by $S^{elm}_{n,T}(\tau_p)$ the output signals by pulsed LIDAR during the convolved pulse duration τ_p ~0.8 ns (JET). Moreover, we will denote by $\sigma^{elm}_{n,T}(\tau_s)$ the Poisson standard variations (see 3.4) as well as by $\sigma^{stray}_{n,T}(\tau_s)$ and $\sigma^{backgr}_{n,T}(\tau_s)$ the standard deviations of photon numbers due to the stray and plasma background illuminations, respectively. Further we will use the standard expression for the SNR given by $SNR \sim S(\tau_{av})/\sigma_S(\tau_{av})$, where $S(\tau_{av})$ is the useful signal, $\sigma_S(\tau_{av})$ is the total standard deviation, τ_{av} is the averaging time. Then, the corresponding estimates of $SNRs$ by both the methods could be expressed by:

$$SNR^{elm}_{n,T}\left(\tau_s\right) \sim \frac{S^{elm}_{n,T}(\tau_s)}{[(\sigma^{elm}_{n,T}(\tau_s))^2 + (\sigma^{stray}_{n,T}(\tau_s))^2 + (\sigma^{backgr}_{n,T}(\tau_s))^2]^{1/2}}, \tag{16a}$$

$$SNR^{elm}_{n,T}\left(\tau_p\right) \sim \frac{S^{elm}_{n,T}(\tau_p)}{[(\sigma^{elm}_{n,T}(\tau_p))^2 + (\sigma^{stray}_{n,T}(\tau_p))^2 + (\sigma^{backgr}_{n,T}(\tau_p))^2]^{1/2}}, \tag{16b}$$

where $\sigma^{elm}_{n,T}(\tau_p)$, $\sigma^{stray}_{n,T}(\tau_p)$ and $\sigma^{backgr}_{n,T}(\tau_p)$ are the standard deviations due to the Poisson, stray light, and background centred fluctuations during the convolved pulse duration τ_p, respectively. Using now the expressions in (16a, b) one could approximately compare both the estimates $SNR^{elm}_{n,T}\left(\tau_s\right)$ and $SNR^{elm}_{n,T}\left(\tau_p\right)$. As mentioned above, assuming equal numbers of emitted photons of equal wavelengths from the CW and Pulsed TS LIDARs in the same plasma, one can accept for the numbers of TS backscattered photons from the same plasma volume to be approximately the same or $S^{elm}_{n,T}\left(\tau_s\right) \sim S^{elm}_{n,T}\left(\tau_p\right)$ during their accumulation times τ_s and τ_p. In this case for standard deviations we obtain to be expressed approximately by $\sigma^{elm}_{n,T}(\tau_s) \sim \sigma^{elm}_{n,T}(\tau_p)$. For the stray light standard deviations one could accept as discussed above approximately $\sigma^{stray}_{n,T}(\tau_s) \sim \sigma^{stray}_{n,T}(\tau_p)$ due to the defocusing of light beams in the CW LIDAR system. For the plasma light we noted above the application of narrower bandwidths filters Fig. 2(a), contributing to an additional reduction of background mean photon numbers in output ELMs signals by the novel method. Moreover, the quite larger integration time by the novel method will additionally contribute to lower levels of centered fluctuations. At these conditions, one could accept for the background standard deviations the estimate $\sigma^{backgr}_{n,T}(\tau_s) \sim \sigma^{backgr}_{n,T}(\tau_p)$. Finally, with an account of the above comparisons of all variables into estimates (16a, b) one could obtain the approximate estimates of the expected $SNRs$ by both the methods or:

$$SNR^{elm}_{n,T}\left(\tau_s\right) \sim SNR^{elm}_{n,T}\left(\tau_p\right). \tag{17}$$

The comparison of both $SNRs$ just demonstrates that the novel method could provide at least a similar performance as the pulsed LIDAR with respect to SNR. These estimates (16)–(17) are sufficient to accept that the novel method by CW laser can offer novel opportunities for linear detection of fast plasma processes on the torus edge with respect to the pulsed TS LIDAR approach.

4. DISCUSSION

It was demonstrated the linear performance of a novel plasma TS diagnostic method consisting in the direct detection of two independently-selected spectral intensities in a backscattering geometry. The optical set-up simplicity offers a variety of different diagnostic applications in large and smaller tokamaks. E.g., the novel method could form the basis of the future development of fast range-resolved edge diagnostic instruments measuring directly and independently at least two plasma parameters. Moreover, in principle, there are no limitations for the method described to be applied to fast density and temperature measurements inside the core plasma at other scattering geometries (e.g., similar to the optical geometry of HRTS instruments). The intermediate signal in equation (4) could be useful in experimental analyses, as it is directly proportional to the product of the electron density and temperature (the electron pressure in non- or low-magnetized plasma as in the pedestal area). The method provides real-time data processing without retrieving algorithms. The possibility of generating alarm signals to control fast processes inside the reactor are also an important advantage of the method.

5. CONCLUSIONS

In this paper, we proposed and analysed by simulations a model of a TS CW LIDAR diagnostic system, meeting the expected performance for direct fast and linear measurement of ELM-mode electron density and temperature time evolution. The time resolution is easily chosen via the ADCs sampling rate. An approach is considered to the instrument calibration by data from two plasma diagnostics, operating in fusion reactors. Calibration expressions are proposed for the case of a stationary ELM time evolution within a given measurement interval by only calculating the standard deviations and mean values of the calibrating series. Calibration expressions are proposed accounting for Poisson fluctuations in the number of photons received. The calibration approach is also efficient in the case of different sampling steps of the output and the calibrating data.

REFERENCES

[1] L. Barrera *et al.*, Inboard and Outboard Electron Temperature Profile Measurements in JET Using ECE Diagnostics, *Plasma Phys. Control. Fusion* (2010) **52** (8) 085010 14, https://doi.org/10.1088/0741-3335/52/8/085010.

[2] E. De la Luna *et al.*, Electron Cyclotron Emission Radiometer Upgrade on the Joint European Torus (JET) Tokamak, *Review of Scientific Instruments* (2004) **75** (10) 3831, http://dx.doi.org/10.1063/1.1781376.

[3] E. De la Luna *et al.*, Impact of Bulk non-Maxwellian Electrons on Electron Temperature Measurements, *Review of Scientific Instruments* (2003) **74** (3) 1414, http://dx.doi.org/10.1063/1.1538354.

[4] John Wesson, *Tokamaks*, Fourth Edition, Oxford University Press, Oxford (2011).

[5] A. W. Leonard, Diagnostics for Edge Pedestal Research, *Review Scientific Instruments* (2004) **75** (10) 3780, http://dx.doi.org/10.1063/1.1790046.

[6] S. Saarelma *et al.*, MHD Stability Analysis of Diagnostic Optimized Configuration Shots in JET, *Plasma Phys. Control. Fusion* (2005) **47** 713, https://doi.org/10.1088/0741-3335/47/5/003.

[7] D. Stoyanov *et al.*, Resolving the Plasma Electron Temperature Pedestal in JET from Thomson Scattering Core LIDAR Data, in: 37^{th} EPS Conference on Plasma Physics (Dublin, Ireland, 2010), Euro-physics Conference Abstracts 34A, P5.133 (European Physical Society, Geneva, 2010).

[8] T. Tokuzawa *et al.*, Developments of Electron Cyclotron Emission Spectroscopy and Microwave Reflectometry on LHD, *Fusion Science and Technology* (2010) **58** (1) 364–374.

[9] M. Brix *et al.*, Upgrade of the Lithium Beam Diagnostic at JET, *Rev. Sci. Instruments* (2010) **81** (10) 10D733.

[10] A. J. H. Donné *et al.*, Chapter 7: Diagnostics, *Nuclear Fusion* (2007) **47** (6) S337–S384.

[11] H. Fajemirokun *et al.*, A New Method for Estimating and Identifying Systematic Error in Thomson Scattering Diagnostics, *Rev. Sci. Instruments* (1990) **61** (10) 2849, http://dx.doi.org/10.1063/1.1141803.

[12] M. N. A. Beurskens *et al.*, ITER LIDAR Performance Analysis, *Rev. Sci. Instruments* (2008) **79** (10) 10E727.

[13] L. Frassinetti *et al.*, Spatial Resolution of the JET Thomson Scattering System, *Rev. Sci. Instruments* (2012) **86** 013506, doi: 10.1063/1.3673467.

[14] O. Naito, H. Yoshida, and T. Matoba, Analytic Formula for Fully Relativistic Thomson Scattering Spectrum, *Physics of Fluids B*: *Plasma Physics* (1993) **5** (11) 4256–4258, http://dx.doi.org/10.1063/1.860593.

[15] L. Gurdev, T. Dreischuh, and D. Stoyanov, Deconvolution of Long Pulse LIDAR Profiles, in: Kr. Jakunczak (Ed.), Lasers – Applications in Science and Industry, InTech, Rijeka, Croatia (2011) 249–276, ISBN: 978-953-307-755-0.

[16] R. M. Measures, *Laser Remote Sensing*, Wiley, New York, USA (1984).

[17] Nonlinear Distortions, www.amplifier.cd/Tutorial/Distortion/non-linear distortion. htm (accessed 03.07.2017).

[18] W. H. Press *et al.*, *Numerical Recipes*, *The Art of Scientific Computing*, Ch.7, Cambridge University Press, New York (1986).

Received February 11, 2022